Spectral filtering for improved pulsed photothermal temperature profiling in agar tissue phantoms

Matija Milanič
Boris Majaron
Jožef Stefan Institute
Jamova 39
SI-1000 Ljubljana, Slovenia

J. Stuart Nelson
University of California
Beckman Laser Institute
Irvine, California 92612-1475

Abstract. We present a systematic experimental comparison of pulsed photothermal temperature profiling utilizing the customary spectral band of the InSb radiation detector ($\lambda = 3.0$ to 5.6 μm) and a narrowed acquisition band (4.5 to 5.6 μm). We use custom tissue phantoms composed of agar gel layers separated by thin absorbing layers. The laser-induced temperature profiles are reconstructed within the customary monochromatic approximation, using a custom minimization algorithm. In a detailed numerical simulation of the experimental procedure, we consider several acquisition spectral bands with the lower wavelength limit varied between 3.0 and 5.0 μm (imitating application of different long-pass filters). The simulated PPTR signals contain noise with amplitude and spectral characteristics consistent with our experimental system. Both experimental and numerical results indicate that spectral filtering reduces reconstruction error and broadening of temperature peaks, especially for shallower and more complex absorbing structures. For the simulated PPTR system and watery tissues, numerical results indicate an optimal lower wavelength limit of 3.8 to 4.2 μm. © *2008 Society of Photo-Optical Instrumentation Engineers.* [DOI: 10.1117/1.2998477]

Keywords: pulsed photothermal radiometry (PPTR); temperature depth profiling; image reconstruction; infrared absorption.

Paper 08058R received Feb. 18, 2008; revised manuscript received Jul. 8, 2008; accepted for publication Aug. 19, 2008; published online Nov. 5, 2008.

1 Introduction

Photothermal radiometric techniques utilize time-resolved acquisition of infrared (IR) radiation from a laser-irradiated sample to obtain specific information about the sample. For example, the laser-induced temperature profile can be reconstructed from the transient radiometric signal, provided that the optical and thermal properties of the sample are known.[1] Such pulsed photothermal radiometric (PPTR) temperature profiling allows noninvasive determination of chromophore distribution in optically scattering biological tissues, such as human skin.[2,3]

To the best of our knowledge, all reported photothermal radiometric techniques reduce the computational complexity of signal analysis by utilizing a fixed IR absorption coefficient of the sample, although broadband acquisition of IR radiation is used almost universally to increase the signal-to-noise ratio (SNR). Application of such monochromatic approximation in soft biological tissues is controversial due to pronounced variation of absorption coefficient $\mu(\lambda)$ in the relevant mid-IR spectral range. Earlier studies have suggested that narrowing of the spectral acquisition band could improve the accuracy of PPTR temperature depth profiling, despite the related decrease of the SNR.[4,5]

Herein, we present a systematic experimental comparison of PPTR temperature profiling utilizing the customary spectral band of the InSb radiation detector ($\lambda = 3.0$ to 5.6 μm) and a narrowed acquisition spectral band (4.5 to 5.6 μm). The measurements were performed in agar tissue phantoms with thin absorbing layers located at various subsurface depths. The laser-induced temperature profiles were reconstructed within the customary monochromatic approximation, with the effective IR absorption coefficient values (μ_{eff}) determined separately for each spectral band.[5]

Our experimental observations are supported by a detailed numerical simulation of the procedure. For initial temperature profiles, resembling those in our agar samples, we compute PPTR signals for several acquisition spectral bands and augment them with noise with amplitude and spectral characteristics consistent with our experimental system. By varying the lower wavelength limit between 3.0 and 5.0 μm (imitating application of different long-pass filters), we can determine the optimal degree of spectral filtering.

2 Theoretical Background

Fundamentals of PPTR temperature profiling can be found elsewhere.[3–6] In its most general form, the transient part of the measured radiometric signal, $\Delta s(t)$, is related to temperature rise in the sample $\Delta T(z,t)$ as[5]

Address all correspondence to: Boris Majaron, Jožef Stefan Institute, Complex Matter, Jamova 39, Ljubljana, 1000, Slovenia. Tel: 386-1-477-3208; Fax: 386-1-423-5400; E-mail: boris.majaron@ijs.si

$$\Delta s(t) = C\varepsilon A \sin^2\theta \int_{\lambda_l}^{\lambda_h} R(\lambda)B_\lambda'(T_b)\mu(\lambda)$$

$$\times \int_{z=0}^{\infty} \Delta T(z,t)\exp[-\mu(\lambda)z]\mathrm{d}z\mathrm{d}\lambda, \qquad (1)$$

where ε is sample emissivity, λ_l and λ_h define the spectral acquisition band, and $B_\lambda'(T_b)$ denotes the temperature derivative of Planck's radiation formula at baseline temperature, T_b. The radiation detector is characterized by its active area (A), half-angle of its field of view (θ), and spectral responsivity, $R(\lambda)$. Constant C accounts for other experimental factors, such as losses of collection optics, etc.

By expressing $\Delta T(z,t)$ after pulsed laser irradiation with the convolution of the initial temperature distribution $\Delta T(z,0)$ and Green's function solution to the one-dimensional heat diffusion equation,[3] integration of the latter and the exponential function $\exp[-\mu(\lambda)z]$ in Eq. (1) can be performed in advance to yield

$$\Delta s(t) = C\varepsilon A \sin^2\theta \int_{\lambda_l}^{\lambda_h} R(\lambda)B_\lambda'(T_b)\int_{z=0}^{\infty}\kappa_\lambda(z,t)\Delta T(z,0)\mathrm{d}z\mathrm{d}\lambda. \qquad (2)$$

For a semi-infinite medium and convective/radiative boundary condition, the monochromatic kernel function $\kappa_\lambda(z,t)$ assumes the form[3]

$$\kappa_\lambda(z,t) = \frac{1}{2}\mu(\lambda)\exp(-z^2/4Dt)\Big\{\mathrm{erfcx}(u_-) + \mathrm{erfcx}(u_+)$$

$$+ \frac{2h}{\mu(\lambda)-h}[\mathrm{erfcx}(u_+) - \mathrm{erfcx}(u_1)]\Big\}, \qquad (3)$$

where $\mathrm{erfcx}(u)=\exp(u^2)\mathrm{erfc}(u)$ is the exponential complementary error function, $u_\pm=\mu(\lambda)\sqrt{Dt}\pm z/\sqrt{4Dt}$, and $u_1=h\sqrt{Dt}+z/\sqrt{4Dt}$. D and h denote the sample thermal diffusivity and reduced heat transfer coefficient at its surface, respectively.

Prior to signal analysis, we calibrate the radiometric signals by fitting the values obtained from a homogeneous black body with varying temperature with Planck's radiation formula. By using the obtained calibration curve, each radiometric signal value can then be converted to the temperature of the black body producing the same signal (also known as radiometric temperature). Performing such calibration removes most of the error induced by linearization of the Planck's radiation law in Eq. (1). In addition, it eliminates the experimentally specific prefactors in Eqs. (1) and (2), thus enabling absolute measurements of temperature rise in the sample. While a thorough analysis of the calibration procedure is beyond the scope of this article,[7] the latter effect can be easily derived by setting the amplitude of the calibrated signal (ΔS) equal to the spatially uniform temperature rise (ΔT) within the linear approximation of Eq. (1):

$$\Delta S = \frac{\Delta s}{C\varepsilon A \sin^2\theta\int_{\lambda_l}^{\lambda_h}R(\lambda)B_\lambda'(T_b)\mathrm{d}\lambda}. \qquad (4)$$

From Eqs. (2) and (4), the calibrated PPTR signal transient $\Delta S(t)$ equals

$$\Delta S(t) = \int_{z=0}^{\infty} K(z,t)\Delta T(z,0)\mathrm{d}z, \qquad (5)$$

where the spectrally composite kernel function $K(z,t)$ has the form

$$K(z,t) = \frac{\int_{\lambda_l}^{\lambda_h}R(\lambda)B_\lambda'(T_b)\kappa_\lambda(z,t)\mathrm{d}\lambda}{\int_{\lambda_l}^{\lambda_h}R(\lambda)B_\lambda'(T_b)\mathrm{d}\lambda}. \qquad (6)$$

Experimental PPTR signals are represented by vectors S with components $S_i=\Delta S(t_i)$. Hence, Eq. (5) becomes multiplication of the initial temperature profile, T [$T_j=\Delta T(z_j)$], with a kernel matrix K [$K_{i,j}=K(z_i,t_j)\Delta z$]:

$$S = KT. \qquad (7)$$

Reconstruction of T from a PPTR signal S presents a severely ill-posed problem.[3] Because an exact solution does not exist, the best approximate solution is commonly obtained by minimization of the residual norm, $\|S-KT\|^2$.

3 Tissue Phantom Experiments

3.1 Materials and Methods

3.1.1 Agar gel tissue phantoms

Our test samples are composed of two or three agar gel layers (2.5 wt % agar, 97.5% water), separated by very thin absorbing layers. Details of the agar layer preparation were presented elsewhere.[8] Powdering the agar gel layer surface with fine carbon black powder produced stable, thin layers with high optical absorption.

Three tissue phantoms evaluated in this study (samples A to C) consisted of a 1- to 2-mm-thick gel substrate, thin absorbing layer, and one superficial gel layer of varying thickness. Thus, the subsurface depths of the absorbing layers were approximately 130, 280, and 450 μm, which corresponds to the location of the vascular network in shallow, medium, and deep port-wine stain birthmarks, respectively. One tissue phantom (sample D) included two absorbing layers at approximate depths of 240 and 440 μm. In this sample, fine TiO_2 powder was homogeneously dispersed in the substrate to enhance optical scattering. The increased light fluence in the deeper absorbing layer produced two temperature peaks with comparable amplitudes, despite the attenuation of incident laser light by the upper absorbing layer.[9]

3.1.2 Experimental setup

For each PPTR measurement, the sample was irradiated with a single 1.5-ms-long 585-nm pulse from a pulsed dye laser (ScleroPlus, Candela, Wayland, Massachusetts). Radiant exposure near the center of a 10-mm-diam laser spot was ~3 J/cm^2. Radiation emitted from the center of the irradiated area was collected on the focal-plane array of a fast IR camera (Phoenix, Indigo, Santa Barbara, California) using a macro IR
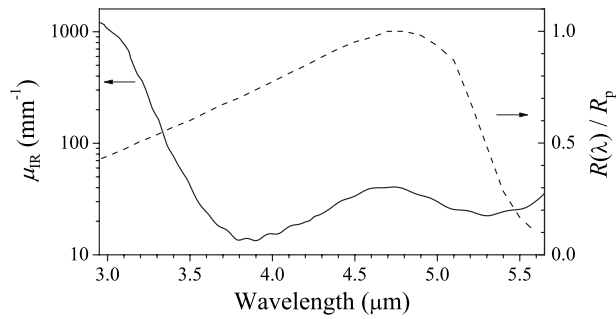
Fig. 1 Absorption coefficient of the agar gel in the mid-IR spectral region (solid line) and responsivity of a typical InSb detector (relative to its peak responsivity R_p; dashed line).

Fig. 2 PPTR signals acquired from agar gel samples A and C using the entire spectral band ($\lambda = 3.0$ to 5.6 μm; thinner lines) and narrowed spectral band (4.5 to 5.6 μm; heavy lines).

objective with magnification $M=1$. By limiting the data read-out to a 128×64 pixel subwindow and setting the integration time to $t_{int}=0.5$ ms, the acquisition rate was 1083 frames per second. The acquisition time was set to 1 s after the laser pulse.

Radiometric signals were obtained from three different sites on each sample, separated by a few millimeters. This ensures that the influence of residual heat on successive measurements is negligible. On each test site, up to three radiometric signals were acquired, first utilizing the entire spectral band of the IR camera ($\lambda = 3.0$ to 5.6 μm) and then with a custom long-pass IR filter (cut-on at 4.5 μm, Barr Associates, Westford, Massachusetts) fitted to the collection optics.[4] The response of each array element was calibrated using a computer-controlled black body (BB701, Omega Engineering, Stamford, Connecticut) as described earlier. Last, the PPTR signals S were obtained by averaging the data from 40×40 detector elements (active area $A = 1.2 \times 1.2$ mm^2) and subtracting the baseline value.

3.1.3 *Reconstruction of temperature profiles*

The initial temperature profiles T were reconstructed using the customary monochromatic approximation. Elements of the monochromatic kernel matrix, $K = \kappa_\lambda$, were calculated using the thermal parameter values $D = 0.134$ mm^2/s and $h = 0.02$ mm^{-1}. The effective absorption coefficient was determined from IR spectral properties of the sample and radiation detector (Fig. 1) by following a recently presented analytical approach.[5] The obtained values were $\mu_{eff} = 28.0$ mm^{-1} for the full spectral band ($\lambda = 3.0$ to 5.6 μm) and $\mu_{eff} = 30.2$ mm^{-1} for the narrowed spectral band (4.5 to 5.6 μm).

The initial temperature profiles were reconstructed using a custom iterative minimization code on a personal computer. The code combines the conjugate-gradient algorithm with non-negativity constraint to the temperature vector components and automated adaptive regularization.[10] The results consist of 140 temperature values over a depth range of 0.7 mm (discretization step $\Delta z = 5$ μm).

3.2 *Experimental Results*

Figure 2 presents PPTR signals acquired from samples A and C using the full-spectrum and narrowed-spectrum acquisition (thinner and heavier lines, respectively). Experimental noise is evident, particularly in the latter case. The noise-equivalent
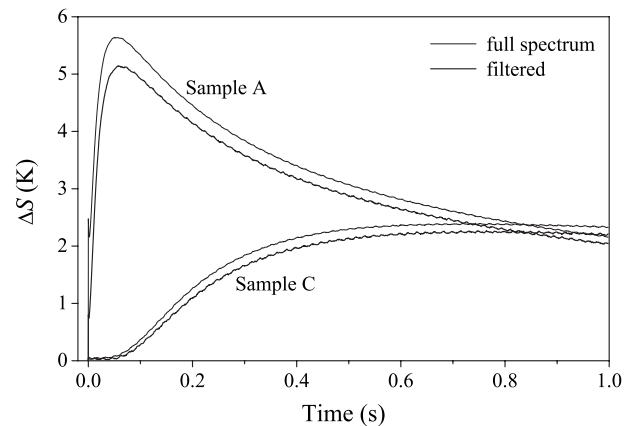
temperature rise, determined as the standard deviation of radiometric signals before laser exposure, amounts to $NE\Delta T = 6.5$ and 10.9 mK for the full- and narrowed-spectrum acquisition, respectively. Average SNR values for all measured PPTR signals are summarized in Table 1.

Figure 3 shows temperature profiles reconstructed from PPTR measurements on three different sites in samples A to D, using the entire spectral band of the IR camera (dashed lines) and spectrally filtered acquisition (solid lines). Peak temperature depths determined on the same site with the two approaches do not differ significantly. The observed variation of the depth between different sites in the same sample is likely due to nonuniform thickness of the superficial gel layer.

More importantly, however, temperature profiles obtained with the narrowed-spectrum acquisition on average appear narrower than the full-spectrum results. As illustrated in Figure 4, the average full widths at half maximum (W) of the temperature profiles reconstructed from narrowed-spectrum PPTR signals are indeed smaller as compared to the full-spectrum results, for all five absorption layers. This indicates that spectral filtering reduces the broadening in the reconstructed PPTR temperature profiles.

Table 1 Signal-to-noise ratios (SNRs) for PPTR signals obtained from four agar gel samples (A to D) using full—(middle column) and narrowed-spectrum (right column) acquisition.

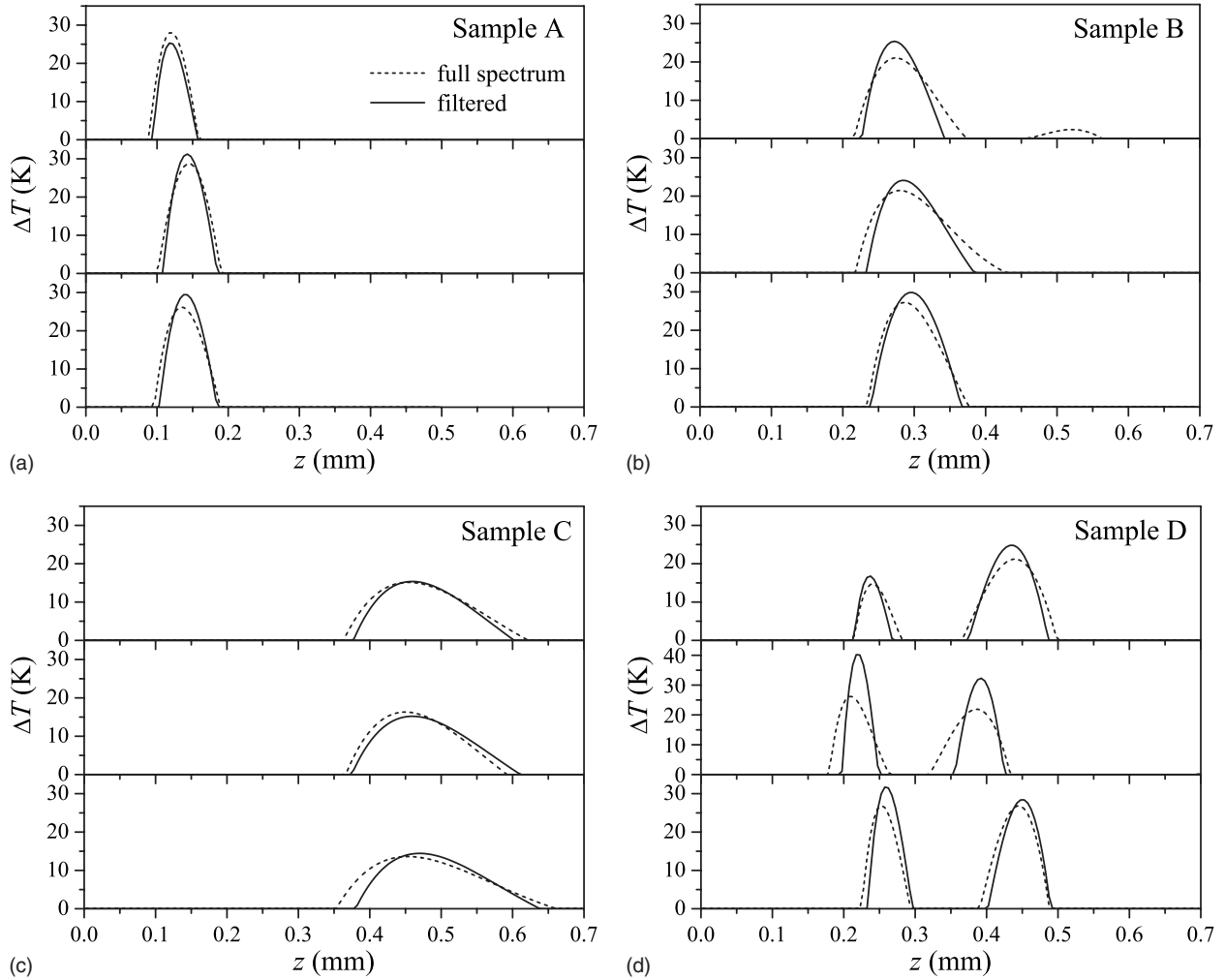| Sample	$\lambda = 3.0$ to 5.6 μm	$\lambda = 4.5$ to 5.6 μm
A	496	245
B	456	285
C	295	155
D	482	277

Fig. 3 Reconstructed temperature profiles for three sites on samples A to D, obtained using the full-spectrum ($\lambda = 3.0$ to 5.6 μm; dashed lines) and narrowed-spectrum signal acquisition ($\lambda = 4.5$ to 5.6 μm; solid lines).

4 Numerical Simulation

4.1 Methods

For correspondence with some earlier studies,[4,5,10] the initial temperature profiles in our numerical simulation have a so-called hyper-Gaussian form: $\Delta T(z, 0) = \Delta T_0 \exp[-2(z - z_0)^4 / w_0^4]$ (see Fig. 5, dashed line). To resemble our experimental data, we select the parameter values $\Delta T_0 = 30$ K and $w_0 = 30$ μm and set z_0 to 133 μm (test object A), 282 μm (B), or 468 μm (C). An additional test profile is composed of two hyper-Gaussian lobes of width w_0 centered at $z_1 = 223$ μm and $z_2 = 403$ μm (object D). The corresponding vectors T_0 consist of 140 values evaluated at equidistant depths over a depth of 0.7 mm.

The theoretical signals vectors S_0 are calculated from T_0 using Eq. (7). These have 1083 components and represent PPTR signal values acquired at a sampling rate of 1083 s^{-1}. To study the influence of the spectral acquisition band on performance of the PPTR system, we vary the lower wavelength limit λ_l from 3.0 to 5.0 μm, while the upper wavelength limit is fixed at the InSb radiation detector cutoff wavelength, $\lambda_h = 5.6$ μm. The corresponding kernel matrices K are

calculated by dividing each spectral acquisition band into N intervals of width 0.02 μm and adding up their contributions in accordance with Eq. (6):

$$K_{i,j} = \sum_{n=1}^{N} R(\lambda_n) B'_{\lambda_n}(T_b) \kappa_n(z_j, t_i; \mu_n) \bigg/ \sum_n R(\lambda_n) B'_{\lambda_n}(T_b).$$

(8)

Here, λ_n is the central wavelength of the nth spectral interval, and μ_n is the corresponding IR absorption coefficient of the agar gel (Fig. 1).

4.1.1 Noise

For additional realism of the simulation, the theoretical PPTR signals S_0 are augmented by noise. Multiple sources contribute to noise in IR detection. Shot noise, which originates from the discrete nature of the photodetection process, has the amplitude[11]
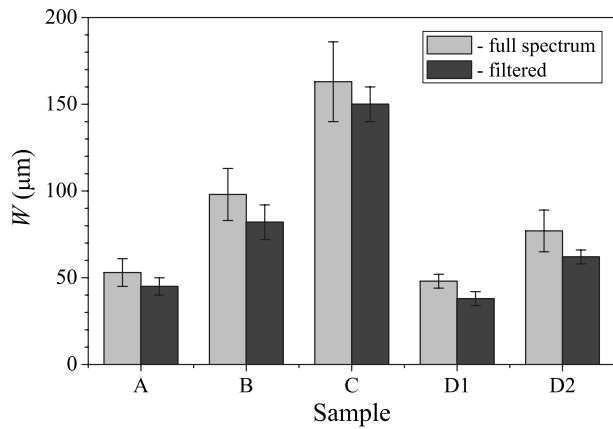
Fig. 4 Average widths of the temperature peaks in agar test samples A to C and both absorption layers in sample D (marked D1 and D2) as determined using the full-spectrum (light gray) and filtered PPTR (dark gray) signal acquisition.

$$n_{sh} = (2e_0 i \Delta f)^{1/2}, \qquad (9)$$

where e_0 represents the electron charge, $\Delta f = (2t_{int})^{-1}$ is frequency bandwidth, and signal i can be estimated by

$$i = C\varepsilon A \sin^2\theta \int_{\lambda_l}^{\lambda_h} R(\lambda) B_\lambda(T_b) \mathrm{d}\lambda. \qquad (10)$$

Because the remaining noise contributions do not depend on signal amplitude i, we refer to their sum as detector noise, n_d.[3,11] The total noise amplitude n_t can then be estimated as

$$n_t^2 = n_{sh}^2 + n_d^2. \qquad (11)$$

In the following, we apply the parameters of our experimental system ($A = 1.44$ mm², $\theta = 11.3$ deg, $t_{int} = 0.5$ ms) and $T_b = 298$ K. Peak responsivity of InSb radiation detectors is around $R_p = 3.0$ A/W, and a typical spectral responsivity

$R(\lambda)$ is presented in Fig. 1.[12] For simplicity, we set both ε and C to 1, because their influence on the simulation results is minimal.

Using the well-known relation,[11] which follows directly from Eq. (4),

$$NE\Delta T = \frac{n_t}{C\varepsilon A \sin^2\theta \int_{\lambda_l}^{\lambda_h} R(\lambda) B'_\lambda(T_b)\mathrm{d}\lambda}, \qquad (12)$$

we can compute the total noise amplitude (n_t) from the two experimentally determined $NE\Delta T$ values (6.5 and 10.9 mK for the spectral bands with $\lambda_l = 3.0$ μm and 4.5 μm, respectively). The result, $n_t = 300$ pA, is almost identical for both spectral bands. This is consistent with the fact that the shot noise amplitudes computed for the same spectral bands using Eqs. (9) and (10) are much smaller in comparison ($n_{sh} = 20$ pA and 17 pA, respectively). Because detector noise obviously dominates in our PPTR signals, we can apply the preceding noise amplitude n_t for all simulated spectral bands and compute the corresponding $NE\Delta T$ values using Eq. (12).

While most noise contributions are spectrally invariant ("white"), our radiometric signals also contain so-called $1/f$ noise,[11] characterized by the corner frequency $f_c = 330$ Hz. In response, we simulate noise that contains appropriate contributions of zero-mean white noise and $1/f$ noise.[7]

4.1.2 Image reconstruction and analysis

Just as in the experimental part, the initial temperature profiles T are reconstructed from simulated PPTR signals using the effective absorption coefficient values μ_{eff} determined separately for each spectral band.[5]

Because the actual initial temperature profiles T_0 are known, we can assess the relative image error δ, defined as
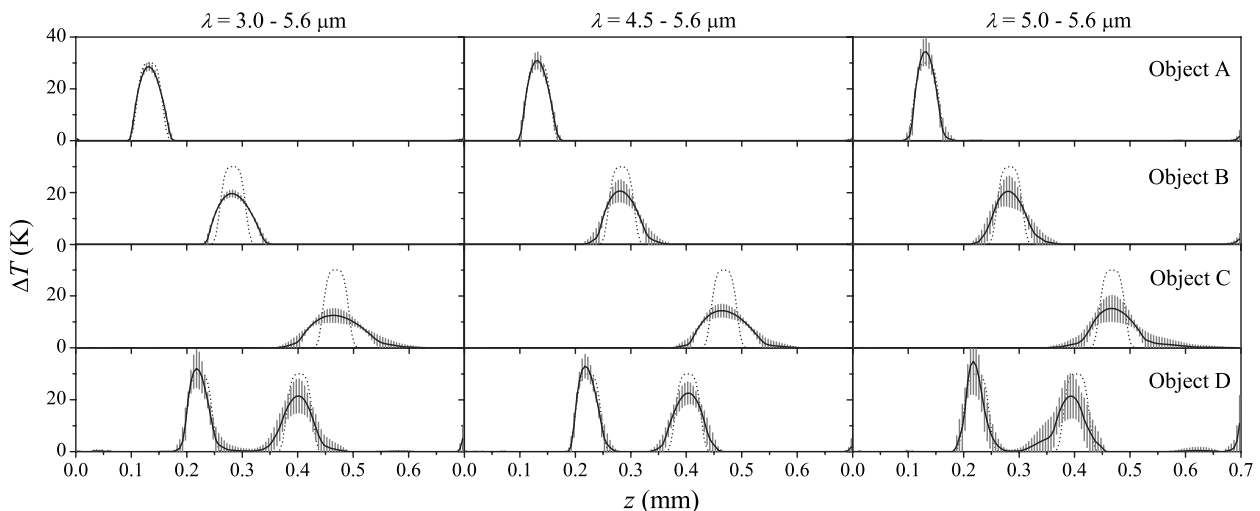

Fig. 5 Images of test objects A (1st row), B (2nd row), C (3rd row), and D (4th row), reconstructed from simulated PPTR signals with spectral bands of $\lambda = 3.0$ to 5.6 μm (left), 4.0 to 5.6 μm (center), and 5.0 to 5.6 μm (right). Solid lines are average temperature profiles, and gray error bars are standard deviations as computed from 10 repetitions with different noise realizations. The actual test objects are plotted for comparison (dashed lines).
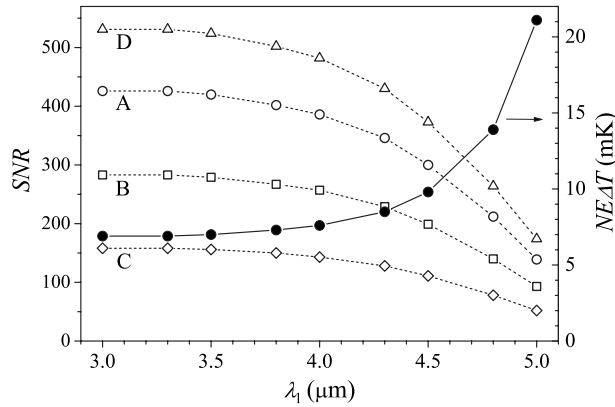
Fig. 6 $NE\Delta T$ (solid circles) and SNR of the simulated PPTR signals for all test objects (open symbols) as a function of the lower wavelength limit, λ_l.

$$\delta = \frac{\|T - T_0\|}{\|T_0\|}. \qquad (13)$$

The reconstruction results are sensitive to specific noise realizations, so each theoretical signal S_0 (corresponding to a particular combination of the initial temperature profile and spectral band) is augmented with 10 different realizations of noise, and the results are analyzed statistically.

4.2 Simulation Results

Figure 6 presents the $NE\Delta T$ values [Eq. (12)] as a function of the lower wavelength limit of the acquisition spectral band, λ_l (solid circles). Evidently, spectral narrowing increases $NE\Delta T$ from 6.9 mK at $\lambda_l=3.0$ μm to 21.1 mK at $\lambda_l=5.0$ μm. Consequently, the SNR decreases with increasing λ_l for all test objects (open symbols).

The effective IR absorption coefficients as computed for the involved spectral bands are presented in Fig. 7. The values vary between $\mu_{eff}=25.0$ mm^{-1} and 30.2 mm^{-1}, as dictated by spectral dependences $\mu(\lambda)$, $R(\lambda)$, and $B'_\lambda(T_b)$.

Figure 5 presents statistical analysis of the reconstructed temperature profiles ("images") for three spectral acquisition bands: $\lambda=3.0$ to 5.6 μm (left column), 4.5 to 5.6 μm (center), and 5.0 to 5.6 μm (right). In each graph, the solid line
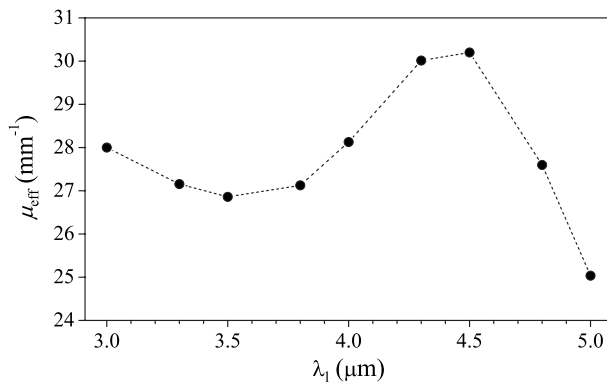

Fig. 7 Effective IR absorption coefficient (μ_{eff}) as a function of the lower wavelength limit, λ_l. The upper limit λ_h is fixed at 5.6 μm.

connects the average temperature values, and vertical bars indicate their standard deviations. The actual test profiles are depicted for comparison (dashed lines).

The reconstructed images of object A (top row) are evidently broader and lower for the full spectral band (left) as compared to either narrowed spectral band (center, right). However, narrowing of the spectral band compromises the stability of the reconstruction result due to reduced SNR. Similar trends are observed also for objects B and C (second and third rows, respectively). For object D (bottom row), moderate spectral filtering ($\lambda=4.5$ to 5.6 μm; center) evidently results in most accurate reconstruction of the deeper temperature lobe, the smallest standard deviations, and least pronounced artifact at the deep end of the reconstruction interval.

Figure 8(a) presents relative image errors (δ) as a function of λ_l for all test objects. For object A (circles), the minimal average error is obtained at $\lambda_l=3.8$ μm ($\delta=0.088$; note the arrow). For λ_l above 4.0 μm, δ increases due to decreasing SNR, up to $\delta=0.19$ at $\lambda_l=5.0$ μm. On the other hand, the image error also increases when λ_l is reduced below 3.8 μm (reaching $\delta=0.14$ at $\lambda_l=3.0$ μm), due to increasing deficiency of the monochromatic approximation. Moreover, the same trend is evident also for standard deviation of δ, which is minimal at $\lambda_l=3.8$ μm ($\sigma_\delta=0.02$) and markedly larger for both broader (e.g., $\sigma_\delta=0.05$ at $\lambda_l=3.0$ μm) and narrower spectral acquisition bands ($\sigma_\delta=0.10$ at $\lambda_l=5.0$ μm).

Similar to the preceding, the minimal relative error for object B [Fig. 8(a), squares] is found at $\lambda_l=3.8$ μm ($\delta=0.36$), and the values increase for both broader and narrower spectral bands. All image errors are much larger as compared to object A, due to the larger depth z_0 of absorption layer in object B. The standard deviation tends to increase with spectral narrowing ($\sigma_\delta=0.04$, 0.08, and 0.19 at $\lambda_l=3.0$, 3.8, and 5.0 μm, respectively). The image errors for object C are even larger than for object B and tend to decrease with spectral narrowing [Fig. 8(a), diamonds]. However, this trend is almost concealed by large standard deviations σ_δ, which tend to increase with λ_l.

The results for the two-lobed object D [Fig. 8(a), bottom] indicate a minimal image error at $\lambda_l=4.0$ μm ($\delta=0.27\pm0.9$; arrow). However, in view of the large standard deviations, λ_l between 3.5 and 4.5 μm can be considered equally adequate. Outside of this range, both δ and σ_δ tend to increase, especially toward $\lambda_l=5.0$ μm.

As demonstrated in Fig. 8(b), the reconstructed temperature profiles are usually broader than the test objects ($W=47$ μm; note the dashed line). For test object A (circles) the optimal result is fairly close ($W=51$ μm; arrow). The optimal spectral filtering ($\lambda_l=3.8$ to 4.0 μm) is the same as indicated by analysis of the image errors in Fig. 8(a), although the minimum is less pronounced. The image widths W increase in particular for broader spectral bands (i.e., lower λ_l), while standard deviations σ_W increase when λ_l is changed from the optimal range in either direction (but more so toward higher λ_l).

The reconstructed images of test objects B and C (squares and diamonds, respectively) are much broader than for object A. The closest match ($W=72$ μm and 111 μm, respectively) is obtained at $\lambda_l=4.0$ μm, and the general trends are the same
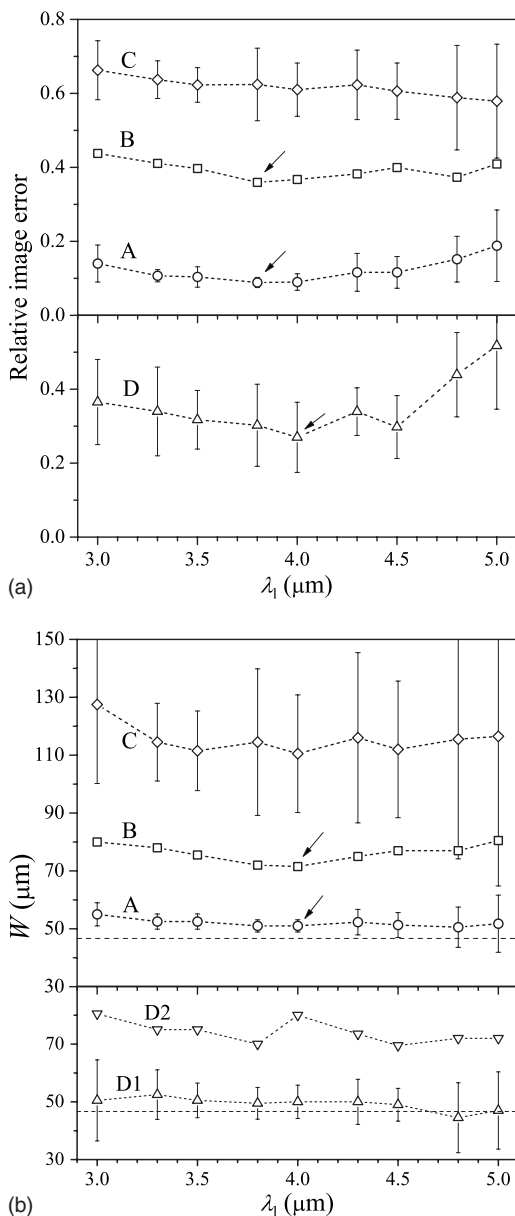
Fig. 8 (a) Relative image error (δ), and (b) full width at half maximum of the reconstructed temperature lobes (W) as a function of the lower wavelength limit λ_l for test objects A (circles), B (squares), C (diamonds), and D (triangles). Standard deviations are plotted for some data sets (bars), and arrows mark distinct minimums. In (b), the widths of both temperature lobes are presented for object D (bottom panel); dashed lines indicate the actual object width.

as observed for object A, although they are almost concealed by large standard deviations.

For the two-lobed test object D [Fig 8(b), bottom], the results from the first peak (up triangles) suggest the optimal value around λ_l=3.5 to 4.5 μm, if both the width W and its standard deviation are considered. For the second peak (down triangles), the trends in $W(\lambda_l)$ are concealed by large standard deviations.

Average peak temperature depths Z and widths W are compared in Table 2 for all test objects and spectral bands with λ_l=3.0 μm (unfiltered), 4.0 μm (near-optimal), and 4.5 μm

(as used in our experiments). The depths Z deviate from the actual central depths z_0 by 1% (object C) or less (objects A, B, and D2), and $\sim$2% for the first peak of object D, regardless of the spectral acquisition band.

In contrast, spectral filtering has a larger effect on image width, W. As illustrated in Fig. 9, the reconstructed images are on average broader and more sensitive to the presence of noise when using the full spectral band (λ_l=3.0 μm) as compared to either narrowed spectral band (λ_l=4.0 μm or 4.5 μm), for all test objects. The difference between the latter results is rather small, although the near-optimal spectral band (λ_l=4.0 μm) on average yields somewhat smaller widths W and standard deviations σ_W.

Quality of the reconstructed image is in general affected by two independent effects, deficiency of monochromatic approximation and presence of noise in PPTR signals. To analyze their respective roles, we compare the results for test object A with the amplitude ΔT_0 varied from 5 K to 60 K. With λ_l varied between 3.0 μm and 5.0 μm, the SNR in simulated PPTR signals ranges from 23 to 71 at ΔT_0=5 K, in contrast with SNR=289 to 851 at ΔT_0=60 K.

As seen in Fig. 10, only the reconstruction of object with ΔT_0=5 K (down triangles) is optimal when using the entire spectral band (λ=3.0 to 5.6 μm). This happens because reconstruction of this object is compromised primarily by the very high noise level. At larger object amplitudes (see the labels in the figure), image errors show minimums when narrowed spectral acquisition bands are used.

5 Discussion

The depths of peak temperature Z as reconstructed from PPTR measurements in tissue phantoms using the full- and narrowed-spectrum signal acquisition are very similar. In samples A and B, the difference is smaller than the applied spatial discretization (Δz=5 μm), and is only slightly larger in samples C and D (Fig. 3). The depths of absorbing layers determined with this PPTR profiling setup were verified earlier using optical coherence tomography (OCT) and histology.[7,8]

These findings are supported by the present numerical simulation, where peak temperature depths Z always deviate from the actual object depths z_0 by less than 2% (Table 2). Our numerical results also confirm that selection of the spectral band does not significantly influence the accuracy of peak temperature depth determination.

Nevertheless, appropriate spectral filtering of PPTR signals does improve the quality of reconstructed temperature profiles. In sample A, temperature profiles reconstructed from the narrowed-spectrum experimental PPTR signals are significantly narrower (W=45$\pm$5 μm) as compared to the full-spectrum acquisition [W=53$\pm$8 μm; Figs. 3(a) and 4]. A similar advantage of spectral filtering is clearly observed in sample D, which features two absorbing layers [Fig. 3(d)]. The effect is least apparent in sample C, with the deepest absorption layer [Fig. 3(c)]. In our experiments, application of spectral filtering has on average reduced the width of reconstructed temperature peaks by 15%, 16%, 8%, 21%, and 20% (for samples A, B, C, and first and second peaks in sample D, respectively) as compared to the full-spectrum approach (Fig. 4).

Table 2 Average depths (Z) and full widths at half maximum (W) of temperature profiles reconstructed from simulated PPTR signals with full ($\lambda = 3.0$ to 5.6 μm), near-optimal (4.0 to 5.6 μm), and the same narrowed spectral band as used in the experiments (4.5 to 5.6 μm). The actual central depths z_0 are given in the first column; the actual width is 47 μm for all test objects.

Sample		z_0 (μm)	$\lambda = 3.0$ to 5.6 μm		$\lambda = 4.0$ to 5.6 μm		$\lambda = 4.5$ to 5.6 μm	
			Z (μm)	W (μm)	Z (μm)	W (μm)	Z (μm)	W (μm)
A		133	133±0	55±4	133±0	51±2	132±1	51±4
B		283	283±0	80±7	282±2	72±8	281±3	77±18
C		468	462±0	128±27	465±3	111±20	464±2	112±24
D	1st	223	218±2	51±14	219±2	50±6	218±3	49±6
	2nd	403	403±5	81±20	405±4	70±13	405±5	72±12

Very similar trends are observed in our numerical results. Especially for test objects A and B, the smallest differences between determined widths W and the actual value are obtained for the narrowed spectral bands with $\lambda_l = 3.8$ to 4.0 μm [Fig. 8(b)]. Across all test objects, the relative reduction of width W with regard to using the full spectral band ($\lambda_l = 3.0$ μm) amounts to 2 to 14%. Standard deviations of the widths are also reduced [Table 2; Figs. 8(b) and 9], indicating that spectral filtering also improves robustness of PPTR temperature profiling, despite the related decrease of SNR.

In the numerical simulations, we could also assess the relative image errors, δ. For objects A, B, and D, δ show distinct minimums at $\lambda_l = 3.8$ to 4.0 μm [Fig. 8(a)] and are not significantly larger at $\lambda_l = 4.5$ μm, used in our experiments. The reduction of δ at $\lambda_l = 4.0$ μm relative to the full-spectrum approach is most prominent for objects A ($\delta = 0.09$ versus 0.14) and D ($\delta = 0.27$ versus 0.37).

Our experimental and numerical results (Figs. 4 and 9; Table 2) confirm earlier reports[6,13] that broadening of the re-

constructed temperature lobes increases nearly proportionally with absorber depth, z_0. In our measurements with spectral filtering, the measured widths W amount to 26 to 36% of z_0 in samples A to C and 11 to 20% of z_0 for the two temperature lobes in sample D (Fig. 4). Note, however, that these widths include the unknown actual thickness of the absorption layer. Moreover, because the radiometric signal is collected from a sizable surface area, they are increased further by the nonuniform depth of the absorption layer[8] and, thus, do not reflect the ultimate spatial resolution of our PPTR profiling setup. If we estimate the broadening effect by subtracting the square of the actual width (47 μm) from the square of determined width W in our numerical simulation results, the result varies between 15% (object A) and 20% (object C) of absorber depth z_0. This is less than reported earlier by Sathyam and Prahl[6] ($W \sim 50\%$ of z_0) or Smithies et al.[13] ($\sim 25\%$).

The adverse effects of noise are dominant for narrow acquisition spectral bands, while the deficiency of monochromatic approximation is most expressed for very broad spectral bands.[5] In general, an optimal spectral band exists, which yields a minimal reconstruction error and sensitivity to experi-
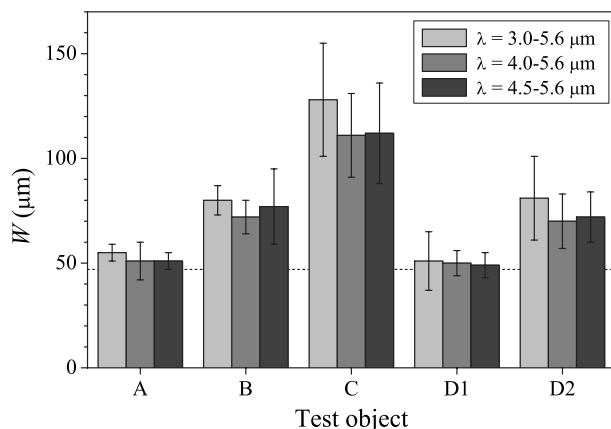
Fig. 9 Comparison of temperature lobe widths W in reconstructed profiles for all test objects, obtained using the full ($\lambda_l = 3.0$ μm), near-optimal ($\lambda_l = 4.0$ μm), and the same narrowed spectral band as in the experiments ($\lambda_l = 4.5$ μm). Error bars indicate standard deviations; dashed line indicates the actual object width.

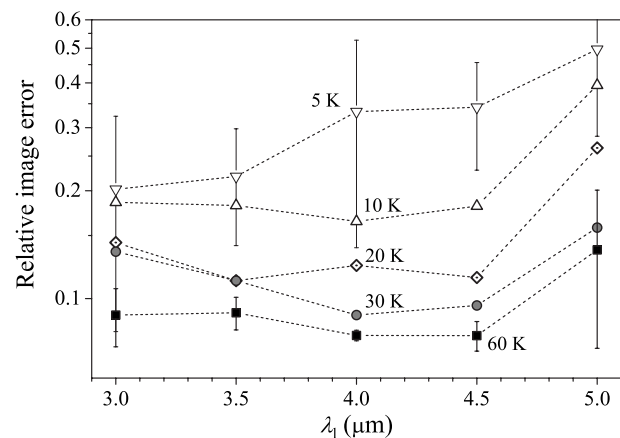**Fig. 10** Relative image error δ as a function of lower wavelength limit λ_l as obtained in numerical simulation with test object A and amplitude ΔT_0 varied between 5 K and 60 K.

mental noise. Our numerical simulations suggest that the spectral bandwith $\lambda_l=3.8$ to 4.2 μm is optimal for the discussed samples and PPTR system (Fig. 8). An exception is presented by the object with $\Delta T_0=5$ K, where the spectral effect is concealed by the very low SNR (Fig. 10).

Based on all of the preceding, we can conclude that appropriate spectral filtering (e.g., $\lambda_l=3.8$ to 4.5 μm) reduces the broadening in reconstructed temperature profiles and improves robustness of PPTR temperature profiling in water-based tissues with SNR values. In general, however, the optimal spectral band will depend on specifics of the sample and experimental system.

For practical reasons and comparison with earlier reports, the present study involved agar tissue phantoms. We believe that our general conclusions are valid also for human skin, because water is the main chromophore in the relevant mid-IR spectral region in both tissues, so their spectral variations $\mu(\lambda)$ are very similar.

Specifically, however, due to the lower water content in skin ($\sim$70%), the correspondingly lower values of μ will make the reconstruction problem slightly more ill-posed as compared to the agar gel.[3] The presented results (e.g., the extent of broadening, optimal spectral bands in relation to absorber depth and temperature rise) may therefore not be transferred directly to the target application. We are currently clarifying the outstanding issues in a follow-up study involving measurements in collagen gel tissue phantoms, which more closely resemble human skin. Meanwhile, the demonstrated performance in agar phantoms and successful measurements *in vivo*[14] indicate that the recent improvements[5,10] may present a viable step toward clinical application of PPTR profiling.

6 Conclusions

In PPTR temperature profiling of agar tissue phantoms, spectral filtering can significantly reduce the broadening of temperature peaks and other image artifacts, especially for shallower and more complex absorbing structures. A suitable amount of spectral filtering is thus beneficial, despite the associated reduction of SNR. For the discussed samples and PPTR system, numerical results indicate an optimal spectral band with $\lambda_l=3.8$ to 4.2 μm. In general, the optimal spectral band depends primarily on the IR spectral properties of the tissue and experimental system specifics.

References

1. F. H. Long, R. R. Anderson, and T. F. Deutsch, "Pulsed photothermal radiometry for depth profiling of layered media," *Appl. Phys. Lett.* **51**, 2076–2078 (1987).
2. S. L. Jacques, J. S. Nelson, W. H. Wright, and T. E. Milner, "Pulsed photothermal radiometry of portwine-stain lesions," *Appl. Opt.* **32**, 2439–2446 (1993).
3. T. E. Milner, D. M. Goodman, B. S. Tanenbaum, and J. S. Nelson, "Depth profiling of laser-heated chromophores in biological tissues by pulsed photothermal radiometry," *J. Opt. Soc. Am. A* **12**, 1479–1488 (1995).
4. B. Majaron, W. Verkruysse, B. S. Tanenbaum, T. E. Milner, and J. S. Nelson, "Spectral variation of infrared absorption coefficient in pulsed photothermal profiling of biological samples," *Phys. Med. Biol.* **47**, 1929–1946 (2002).
5. B. Majaron and M. Milanič, "Effective infrared absorption coefficient for photothermal radiometric measurements in biological tissues," *Phys. Med. Biol.* **53**, 255–268 (2008).
6. U. S. Sathyam and S. A. Prahl, "Limitations in measurement of subsurface temperatures using pulsed photothermal radiometry," *J. Biomed. Opt.* **2**, 251–261 (1997).
7. M. Milanič, "Development and evaluation of pulsed photothermal radiometry for temperature profiling in biological tissues," PhD thesis, Univ. of Ljubljana, Slovenia (2008).
8. M. Milanič, B. Majaron, and J. S. Nelson, "Pulsed photothermal temperature profiling of agar tissue phantoms," *Lasers Med. Sci.* **22**, 279–284 (2007).
9. B. C. Wilson, "Measurement of tissue optical properties: methods and theories," in *Optical-Thermal Response of Laser-Irradiated Tissue*, J. A. Welch, Ed., pp. 233–271, Plenum, New York (1995).
10. B. Majaron and M. Milanič, "Re-evaluation of pulsed photothermal radiometric profiling in samples with spectrally varied infrared absorption coefficient," *Phys. Med. Biol.* **52**, 1089–1101 (2007).
11. J. D. Vincent, *Fundamentals of Infrared Detector Operation and Testing*, Wiley, New York (1989).
12. Judson Technologies, "Indium Antimonide detectors," Product Information, Montgomeryville, PA (2003).
13. D. J. Smithies, T. E. Milner, B. S. Tanenbaum, D. M. Goodman, and J. S. Nelson, "Accuracy of subsurface distributions computed from pulsed photothermal radiometry," *Phys. Med. Biol.* **43**, 2453–2463 (1998).
14. B. Majaron, M. Milanič, and J. S. Nelson, "Interaction of a dual-wavelength laser system with cutaneous blood vessels," in *Therapeutic Laser Applications and Laser-Tissue Interactions III*, A. Vogel, Ed., *Proc. SPIE* **6632**, 66320C (2007).